

# PCCP

Accepted Manuscript



This is an *Accepted Manuscript*, which has been through the Royal Society of Chemistry peer review process and has been accepted for publication.

*Accepted Manuscripts* are published online shortly after acceptance, before technical editing, formatting and proof reading. Using this free service, authors can make their results available to the community, in citable form, before we publish the edited article. We will replace this *Accepted Manuscript* with the edited and formatted *Advance Article* as soon as it is available.

You can find more information about *Accepted Manuscripts* in the [Information for Authors](#).

Please note that technical editing may introduce minor changes to the text and/or graphics, which may alter content. The journal's standard [Terms & Conditions](#) and the [Ethical guidelines](#) still apply. In no event shall the Royal Society of Chemistry be held responsible for any errors or omissions in this *Accepted Manuscript* or any consequences arising from the use of any information it contains.



PCCP

Paper

## Room temperature NO<sub>2</sub> sensing: What advantage does the rGO-NiO nanocomposite have over the pristine NiO?

Received 00th January 20xx,  
Accepted 00th January 20xx

DOI: 10.1039/x0xx00000x

www.rsc.org/

Jian Zhang<sup>a</sup>, Dawen Zeng<sup>a\*</sup>, Shiqian Zhao<sup>b</sup>, Jinjin Wu<sup>a</sup>, Keng Xu<sup>a</sup>, Qiang Zhu<sup>a</sup>, Guozhu Zhang<sup>a</sup> and Changsheng Xie<sup>a</sup>

In recent years, there has been increasing interest in synthesis of reduced graphene oxide (rGO)-metal oxide semiconductor (MOS) nanocomposites for room temperature gas sensing applications. Generally, the sensitivity of MOS can be obviously enhanced by the incorporation of rGO. However, a lack of knowledge regarding how rGO can enhance gas-sensing performances of MOS impedes its sensing applications. Herein, in order to get an insight into the sensing mechanism of rGO-MOS nanocomposites and further improve the sensing performances of NiO-based sensors at room temperature, an rGO-NiO nanocomposite was synthesized. Through a comparison study on room temperature NO<sub>2</sub> sensing of the rGO-NiO and the pristine NiO, an inverse gas-sensing behavior in different NO<sub>2</sub> concentration ranges was observed and the sensitivity of the rGO-NiO was enhanced obviously in the high concentration range (7-60 ppm). Significantly, the stimulating effect of rGO on recovery rate was confirmed by the sensing characteristics of the rGO-NiO that was advantageous for the development of NO<sub>2</sub> sensors at room temperature. Through comprehending the electronic interactions between the rGO-MOS nanocomposite and the target gas, this work may open up new possibilities for further improvement of graphene-based hybrid materials with even higher sensing performances.

### 1. Introduction

Graphene has attracted tremendous attention from both experimental and theoretical perspectives since its discovery in 2004.<sup>1-3</sup> As derivative of graphene, reduced graphene oxide (rGO) inherits the excellent properties of graphene, which is usually composited with a second component for a variety of applications.<sup>4-6</sup> In particular, the unique and outstanding properties of rGO, including low electrical noise and high electron mobility at room temperature, have spurred increasing interest to synthesize the rGO-metal oxide semiconductor (MOS) nanocomposites as room-temperature gas sensors for monitoring of toxic gases.<sup>7-9</sup>

Nitrogen dioxide (NO<sub>2</sub>), released from combustion facilities and automotive engines, is known to be a toxic gas that can cause many diseases and is harmful to environment as a source of acid rain and fog.<sup>10-14</sup> Therefore, in order to meet the practical requirements of NO<sub>2</sub> sensors on low detection limit, high sensitivity, fast recovery rate and low energy consumption, rGO-MOS nanocomposites are widely used for gas sensing, instead of traditional MOS-based sensors. Generally, it has been accepted that most of the

composites of MOS and rGO exhibit the enhanced sensing performances compared to the bare MOS. And most of the related works are inclined to attribute the enhanced sensitivity of rGO-MOS nanocomposites to the contribution of rGO. For example, Srivastava et al. prepared the graphene-WO<sub>3</sub> nanocomposites *via* sol-gel method, and the response to NO<sub>2</sub> increased nearly three times in the case of graphene-WO<sub>3</sub> nanocomposite as compared to the pure WO<sub>3</sub> at room temperature.<sup>15</sup> And it has also been reported that the sensitivity of Cu<sub>2</sub>O mesocrystals grown on rGO sheet toward NO<sub>2</sub> is enhanced at room temperature compared to the pure Cu<sub>2</sub>O mesocrystals.<sup>16</sup> In these graphene-MOS nanocomposites, the incorporated graphene not only can provide the effective conductive matrix, but also can prevent the aggregation of MOS that offers enough active sites for gas adsorption. Therefore, it is generally believed that the composites of rGO anchored with MOS are promising for designing the better performance gas sensors by efficiently utilizing the combinative merits of MOS and rGO.

Although demonstrations of significant improvement in the room temperature sensing performances of rGO-MOS composites are numerous, some important factors, such as the electron transferring at the interface between MOS and rGO, the interactions of gas molecules with nanocomposites *via* chemical or physical adsorption, and the evolution of active sites for effective adsorption, are rarely involved comprehensively. Moreover, rGO contains many dangling bonds and defective sites<sup>17</sup>, which may create a competitive relation with the active sites of MOS for gas adsorption, especially in the case of low level concentration of

<sup>a</sup> State Key Laboratory of Materials Processing and Die Mould Technology, Huazhong University of Science and Technology (HUST), No. 1037, Luoyu Road, Wuhan 430074, China. E-mail: dwzeng@mail.hust.edu.cn; Tel: +86-027-87559835

<sup>b</sup> Aviation Key Laboratory of science and Technology on Precision Manufacturing, P. O. Box 2559, Beijing 100076, China.

testing gas. If the advantages and disadvantages of rGO cannot be taken into account comprehensively, it may give the incomplete or exaggerated information on the contribution role of graphene to enhance the gas-sensing performances of semiconductors. Herein, the knowledge regarding the specific advantage of graphene on how to design or fabricate the efficient rGO-MOS nanocomposite sensors and understand the origin of their enhanced sensing performance is far from satisfactory.

Nickel oxide (NiO), a p-type semiconductor, has been reported as the most promising candidate for detecting NO<sub>2</sub>.<sup>18-20</sup> Therefore, in order to get an insight into the sensing mechanism of rGO-MOS nanocomposites, NiO was employed to composite with rGO for the gas sensing studies. And a careful comparison study between the rGO-NiO nanocomposite and the pristine NiO for room temperature NO<sub>2</sub> sensing had been done. Especially, the rGO-NiO nanocomposite exhibited an inverse gas-sensing behaviour in different NO<sub>2</sub> concentration ranges, as compared to the pristine NiO. Significantly, the stimulating effect of graphene on recovery rate was confirmed by the sensing characteristics of rGO-NiO nanocomposite that was advantageous for the development of room-temperature NO<sub>2</sub> sensor. Furthermore, the mechanism of NO<sub>2</sub> molecule adsorption on rGO-NiO nanocomposite and the electronic interaction in nanocomposites were also discussed in detail. Here, the better understanding on room-temperature sensing mechanism may be helpful to further design the graphene-based nanocomposite for higher sensing performance at room temperature.

## 2. Experimental

### 2.1. Synthesis

Graphene oxide (GO) was prepared by oxidation of graphite powder under acidic conditions according to the modified Hummers method.<sup>21</sup> In a typical process to prepare reduced graphene oxide (rGO)-NiO, 20 mg GO was dispersed in 10 mL N,N-Dimethylformamide (DMF), and the obtained dispersion was sonicated for 30 min. Then 1 g anhydrous nickel chloride and 50 mL distilled water were added into the GO dispersion with magnetic stirring. The pH of mixed solution was then adjusted to 10 by 28% ammonia solutions dropwise. Subsequently, the solution was introduced into a 100 mL autoclave for hydrothermal processing at a temperature of 160 °C for 6 h. The obtained precipitate was collected and washed several times with distilled water and ethanol in order to remove the remaining agents, and then collected by centrifugation at 3500 rpm. The precipitate powders were dried at 80 °C overnight and then calcined at 400 °C in a quartz tube furnace for 3 h under N<sub>2</sub> flow. In this work, the various mass ratios of NiCl<sub>2</sub> (0.2 g, 0.4 g, 0.8 g, 1.0 g, 1.5 g) were employed to composite with GO (20 mg) to obtain the rGO-NiO nanocomposite with different contents of NiO, which were denoted as 0.2Ni-G, 0.4Ni-G, 0.8Ni-G, 1.0Ni-G and 1.5Ni-G respectively. In order to carry out the comparative study, the pristine NiO, the bare rGO and the mechanical mixing rGO/NiO sample were also prepared following the above procedures.

### 2.2. Characterization

The morphologies of samples were observed by field-emission scanning electron microscope (FSEM, FEI Sirion 200). Transmission electron microscope (TEM) and high resolution transmission electron microscope (HRTEM) were performed on a Tecnai G2F20 U-TWIN microscope operated at 200 kV. The phase identification was carried out on an X-ray diffractometer (X'pert PRO; PANalytical B.V.) using CuK<sub>α</sub> radiation in the range from 10° to 90°. The surface compositions and chemical states were examined by X-ray photoelectron spectroscopy (AXISULTRA DLD-600W XPS). The specific surface area and the pore size were determined from N<sub>2</sub> adsorption-desorption isotherms at 77 K, obtained by a BRLSORP analyzer. The specific surface area was calculated from the multipoint adsorption data within the linear segment of the N<sub>2</sub> adsorption isotherms, using Brunauer-Emmett-Teller theory. The pore size distribution was determined from the isotherms by using nonlocal density functional theory.

### 2.3. Gas sensing performance testing

Based on our previous work<sup>22</sup>, a thick film technique was employed to prepare the samples for gas sensing tests. Firstly, 20 mg as-prepared nanocomposites was dispersed into 0.2 mL ethanol, and then ultrasonicated into slurry. A drop (0.1 μL) of the obtained slurry was cast onto the Au interdigital electrode which was preprinted on an alumina substrate and then dried in thermostat at 80 °C for 24 h before sensing tests. Here a testing platform, which had been described in detail in our previous works<sup>22,23</sup>, was employed to evaluate the gas sensing properties of the samples.

An extra temperature-controlling system was applied to make sure the whole gas sensing testing could be operated at room temperature. In order to detail the NO<sub>2</sub> adsorption kinetics on rGO-NiO nanocomposite and further understand the gas-sensing mechanism, the high purity nitrogen (99.99%) was chosen as the carrier gas. At the beginning of testing, the samples were put into the testing chamber, and then the whole testing system was cleaned by nitrogen gas flow for 30 min. By controlling the flow ratio of NO<sub>2</sub> and N<sub>2</sub>, the different concentration of NO<sub>2</sub> were obtained to investigate the related gas-sensing process. And the testing process was detailed as follows. The 1 V bias voltage was loaded at 10 s; the testing gas was injected into the testing chamber at 60 s; the testing gas was off at 300 s; the applied bias voltage was unloaded at 550 s and the testing process was ended at 600 s. It is widely accepted that the complete desorption of NO<sub>2</sub> molecules from NiO-based composites cannot take place at room temperature. In order to remove the remnant NO<sub>2</sub> molecules on the testing samples and make sure the repeatability and reliability of testing, the samples were heated at 80 °C for 24 h to recover to the initial state (a stable and unified conductance value) before each testing process. In this work, the gas-sensing properties were assessed through the response  $(G_g - G_o)/G_o$ . Where,  $G_g$  and  $G_o$  are the electrical conductance in the target gas and in nitrogen, respectively. In order to reveal the recovery rate of the NiO and the rGO-NiO in different NO<sub>2</sub> concentrations, the recovery curves of samples were extracted from the dynamic response-recovery curves, as shown in Fig. 1. Generally, the transient conductance in the recovery process can be expressed as<sup>24-27</sup>,

$$G(t)_{\text{recovery}} \sim G_o \exp\left(-\frac{t}{\tau_{\text{recovery}}}\right) \quad (1)$$

where,  $\tau$  is the time constant of recovery transient curves. Here, eqn (1) was applied to fit the recovery curves. The time constant  $\tau$  obtained from the fitting results was employed to evaluate the recovery rate. Besides, a real recovery time was also defined as the time to recover to 10% of response while the testing gas was off in order to further present the real recovery characteristics of the samples.

### 3. Results and discussion

#### 3.1. Characterization of the pristine NiO and the rGO-NiO nanocomposite

XRD measurements were used to investigate the crystal structures of the rGO-NiO nanocomposite and the pristine NiO, as shown in Fig. 2. Both of their XRD patterns can be indexed into the cubic NiO (JCPDS, ICDD no. 78-0423). Raman spectroscopy is a non-destructive and powerful technique for evaluating the structural properties of graphene, which allows distinguishing graphene from graphite and evaluating crystalline quality and thickness of graphene films, and it is also widely employed for examining the ordered and disordered crystal structures.<sup>28</sup> In order to confirm the existence of graphene, Raman spectroscopy was utilized, as shown in Fig. 3. Three Raman peaks located at about  $500\text{ cm}^{-1}$ ,  $710\text{ cm}^{-1}$  and  $1090\text{ cm}^{-1}$  were observed in both spectra, corresponding to the shaking peaks of NiO. The peak at  $500\text{ cm}^{-1}$  can be assigned to the longitudinal optical (LO) one-phonon (1p) modes of NiO. The peaks at  $710\text{ cm}^{-1}$  and  $1090\text{ cm}^{-1}$  can be ascribed to the two-phonon (2p) modes of 2TO and 2LO, respectively.<sup>29,30</sup> The common characteristics of carbon materials in Raman spectra are the D line and the G line, which are attributed to the  $E_{2g}$  phonon of  $C_{sp^2}$  atoms, and the D line due to the breathing modes of k-point phonons of  $A_{1g}$  symmetry.<sup>31,32</sup> As shown in Fig. 3, the Raman spectrum of the rGO-NiO nanocomposite displays the G line at about  $1587\text{ cm}^{-1}$  and the D line at  $1356\text{ cm}^{-1}$  for graphene.<sup>33,34</sup> The above results confirm the crystalline structures and the components of the pristine NiO and the rGO-NiO nanocomposite.

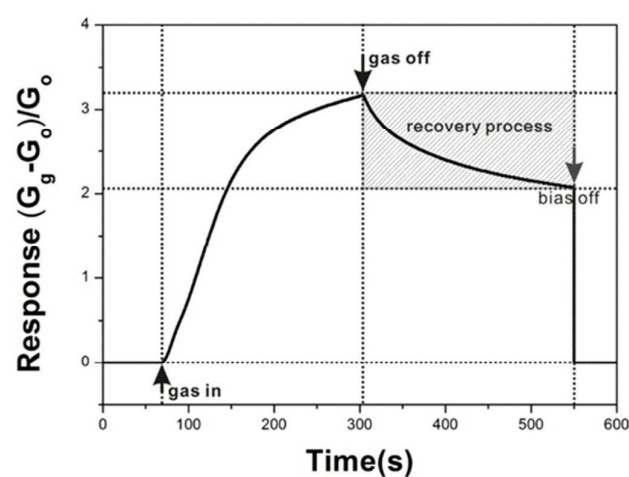


Fig. 1 The dynamic response-recovery curve.

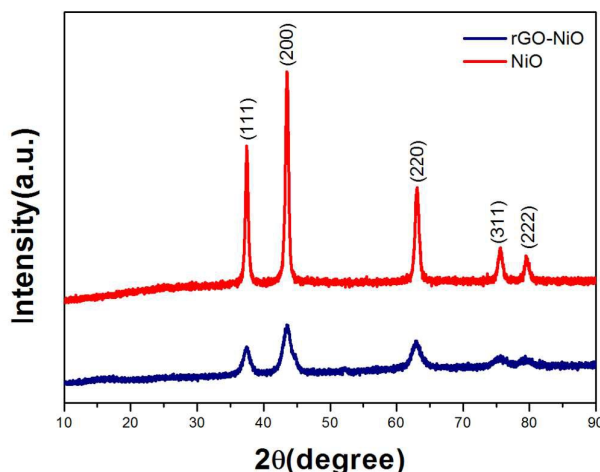


Fig. 2 XRD patterns of the NiO and the rGO-NiO.

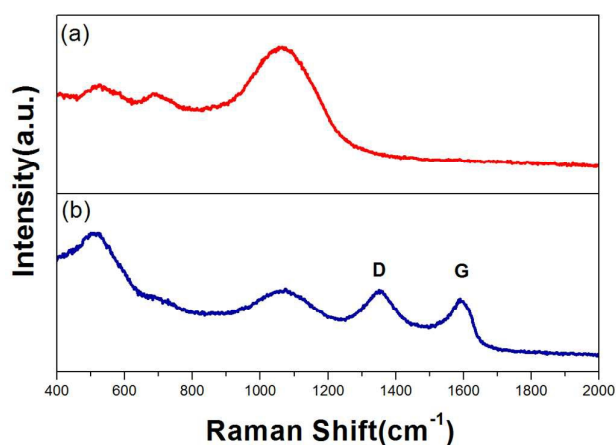


Fig. 3 Raman spectra of the NiO (a) and the rGO-NiO (b).

It is well known that oxygenated graphene films are usually insulating at room temperature, with resistance values on the order of tens of gigaohms ( $G\Omega$ ), due to the disruption of conjugated graphitic structure by epoxide and hydroxyl groups on either side of the graphene basal plane.<sup>35</sup> Therefore, in order to create continuous graphitic paths for charge transport, the oxygen functional groups should be removed. Nethravathi et al. reported that the reduction of graphene oxide could occur at a relatively low temperature in water under solvothermal conditions.<sup>36</sup> Their work opens up an operable one-pot method for us to synthesize rGO-based composites without using any toxic solvents. In order to check whether the GO was reduced to the rGO, XPS was utilized in this work. As C 1s spectra shown in Fig. 4a and b, four peaks centered at 284.5, 285.6, 287.5, 289.0 eV are observed, corresponding to C-C/C=C, C-O, C-O-C/C=O, and O-C=O groups, respectively.<sup>7,37</sup> After reduction, the intensities of C-O and C-O-C/C=O peaks greatly decrease, which is accompanied by an increase of the  $sp^2$  carbon peak (C-C), revealing that a large number of oxygen-containing groups are removed and the majority of the  $sp^2$  carbon networks are restored. Fig. 4c and d show the O 1s spectra obtained from the synthesized rGO-NiO nanocomposite and the mechanical mixed rGO/NiO nanocomposite. The O 1s XPS spectrum

of the mixed rGO/NiO nanocomposite, as shown in Fig. 4d, can be deconvoluted into three peaks. The peak at 529.3 eV corresponds to lattice oxygen in NiO, the peak at 531.0 eV is assigned to HO-C=O groups on rGO or shoulder peak of O 1s in NiO. Compared with the O 1s spectrum of the mixed rGO/NiO, the O 1s spectrum of the synthesized rGO-NiO (Fig. 4c) shifts towards a higher binding energy, indicating the strong interaction between the NiO and the rGO in the synthesized rGO-NiO nanocomposite. Moreover, the extra peak located at 530.2 eV in the O 1s spectrum of the synthesized rGO-NiO nanocomposite is attributed to the possible formation of a Ni-O-C bond<sup>38</sup>, which is beneficial to the electron transfer between the NiO and the rGO.

Fig. 5 shows the typical SEM images of the pristine NiO and the rGO-NiO nanocomposite. As the images of the pristine NiO shown in 5a and b, the pristine NiO consists of the hexagonal nanosheets.

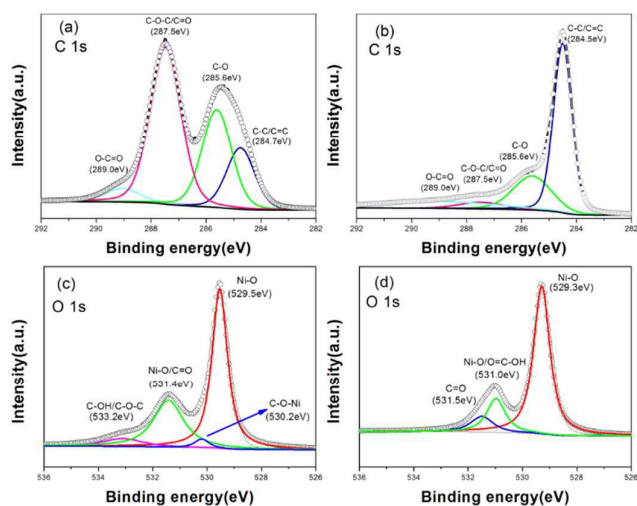


Fig. 4 XPS spectra of (a) GO (C 1s), (b) rGO-NiO (C 1s), (c) rGO-NiO (O 1s), (d) the mechanical mixing rGO/NiO (O 1s).

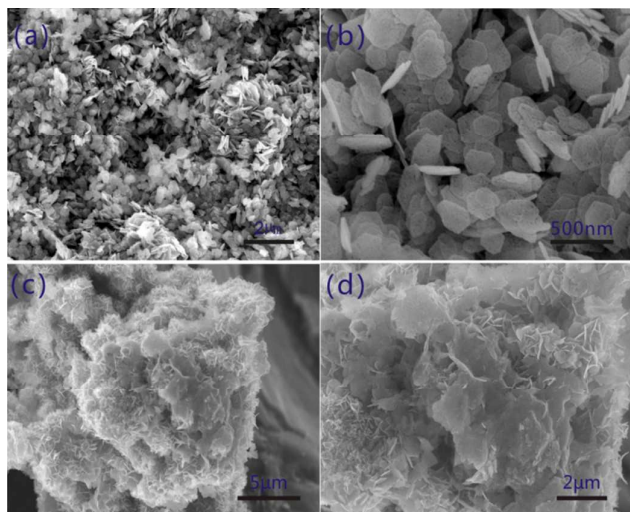


Fig. 5 The low- and high-magnification SEM images of the pristine NiO (a, b); the low- and high-magnification SEM images of the rGO-NiO (c, d).

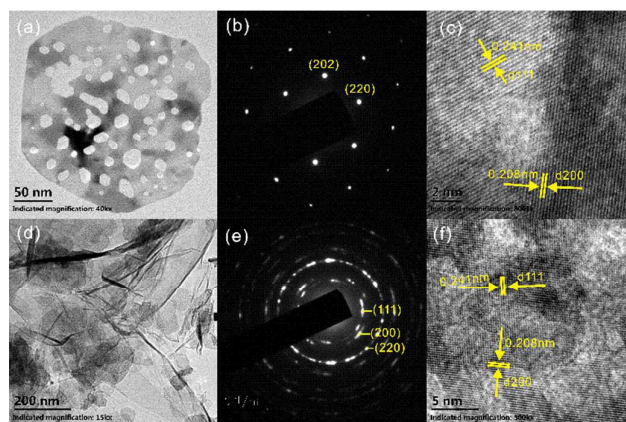


Fig. 6 The TEM images of the NiO (a) and the rGO-NiO nanocomposite (d); the SAED patterns of the NiO (b) and the rGO-NiO nanocomposite (e); the high magnification TEM images of the NiO (c) and the rGO-NiO nanocomposite (f).

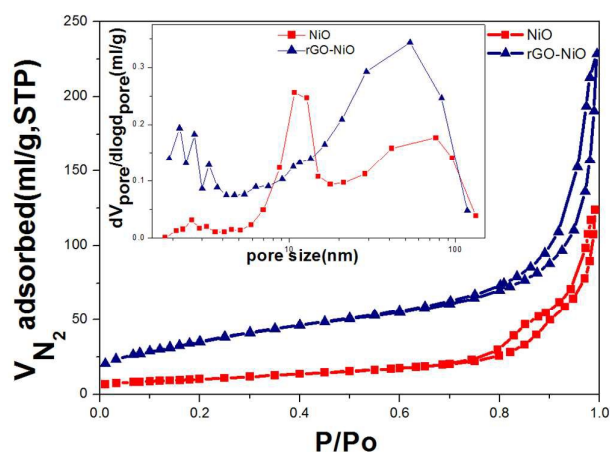
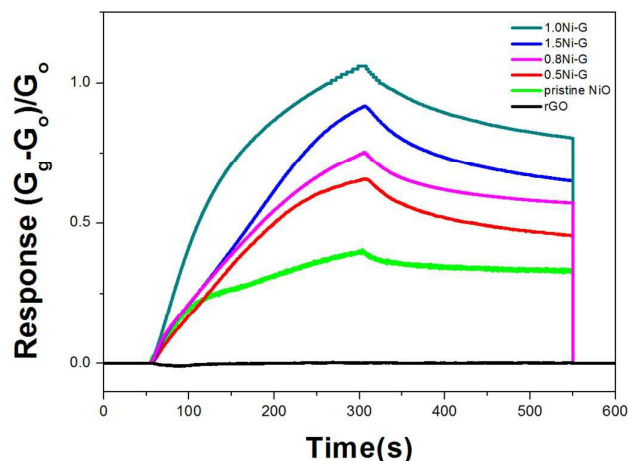


Fig. 7 N<sub>2</sub> adsorption-desorption isotherms (the inset shows BJH pore-size distribution plots of the pristine NiO and the rGO-NiO nanocomposite).

After addition of rGO, the NiO nanosheets are self-assembled on both sides of the rGO in the rGO-NiO nanocomposite, as shown in Fig. 5c and d. In order to provide further insights into their morphologies and structures, the high-resolution photographs were taken by TEM. Evidently, there are many mesopores in the as-prepared NiO nanosheets (Fig. 6a). And the TEM image of the rGO-NiO (Fig. 6d) also identifies that the irregular NiO nanosheets are distributed on the surface of the graphene. The lattice fringes in the HRTEM images of Fig. 6c and f show the interplanar distances of 0.241 nm and 0.208 nm, which can be assigned to the (111) plane and the (200) plane of the hexagonal NiO, respectively. The electron diffraction pattern recorded on a single nanosheet shows the bright spots (Fig. 6b) rather than the rings (Fig. 6e) of the nanocomposite.

The BET surface area and pore size distribution of the NiO and the rGO-NiO were also measured, as shown in Fig. 7. The BET surface area of the rGO-NiO nanocomposite ( $131.74 \text{ m}^2/\text{g}$ ) is  $\sim 3.6$  times higher than that of the pristine NiO nanosheets ( $36.58 \text{ m}^2/\text{g}$ ). Moreover, according to the Barret-Joyner-Halenda (BJH) pore size



**Fig. 8** The dynamic response-recovery curves of the samples with the different mass ratios of NiO and rGO to 15 ppm  $\text{NO}_2$  at room temperature.

distributions of the rGO-NiO and the NiO, the rGO-NiO exhibits the larger mesoporosity in the range of 2-50 nm. The high surface area and the open-pore structure of mesoporous nanocomposite can provide an amplified target-receptor interface, making it an ideal candidate for  $\text{NO}_2$  sensing.

### 3.2. Room-temperature gas sensing properties of the pristine NiO and the rGO-NiO nanocomposite

In order to get the rGO-NiO nanocomposite with better sensing performances, the nanocomposites with the different mass ratios of NiO and rGO were prepared for the gas sensing test. Fig. 8 shows the response transients of the nanocomposites towards 15 ppm  $\text{NO}_2$  at room temperature. The responses of the pristine NiO, 0.5Ni-G, 0.8Ni-G, 1.0Ni-G and 1.5Ni-G are calculated to be 0.39, 0.66, 0.75, 1.1 and 0.92, respectively. With increasing the amount of NiO, the sensitivity is gradually enhanced. And the further increase in the amount of NiO decreases the sensitivity. Here, the bare rGO exhibits no response to  $\text{NO}_2$ , and the response of 1.0Ni-G nanocomposite reaches a maximum value of 1.1.

Based on the above results, 1Ni-G was chosen for the comparative study. And the dynamic response-recovery curves of the pristine NiO and the rGO-NiO nanocomposite against  $\text{NO}_2$  concentration (0.25-60 ppm) are shown in Fig. 9a. In the high concentration range (7-60 ppm), the response of the as-synthesized rGO-NiO nanocomposite is enhanced remarkably compared to the NiO. However, the response of the pristine NiO is even a little higher than that of the rGO-NiO in the low concentration range (0.25-1 ppm). Fig. 9b shows the responses of the pristine NiO and the rGO-NiO nanocomposite versus  $\text{NO}_2$  concentration (0.25-60 ppm) at room temperature. It is apparent that the responses of them increase with increasing  $\text{NO}_2$  concentration. Here, eqn (1) is employed to evaluate the recovery rates by fitting the recovery curves of the pristine NiO and the rGO-NiO. The fitted time constants of the NiO are larger than the time constants of the

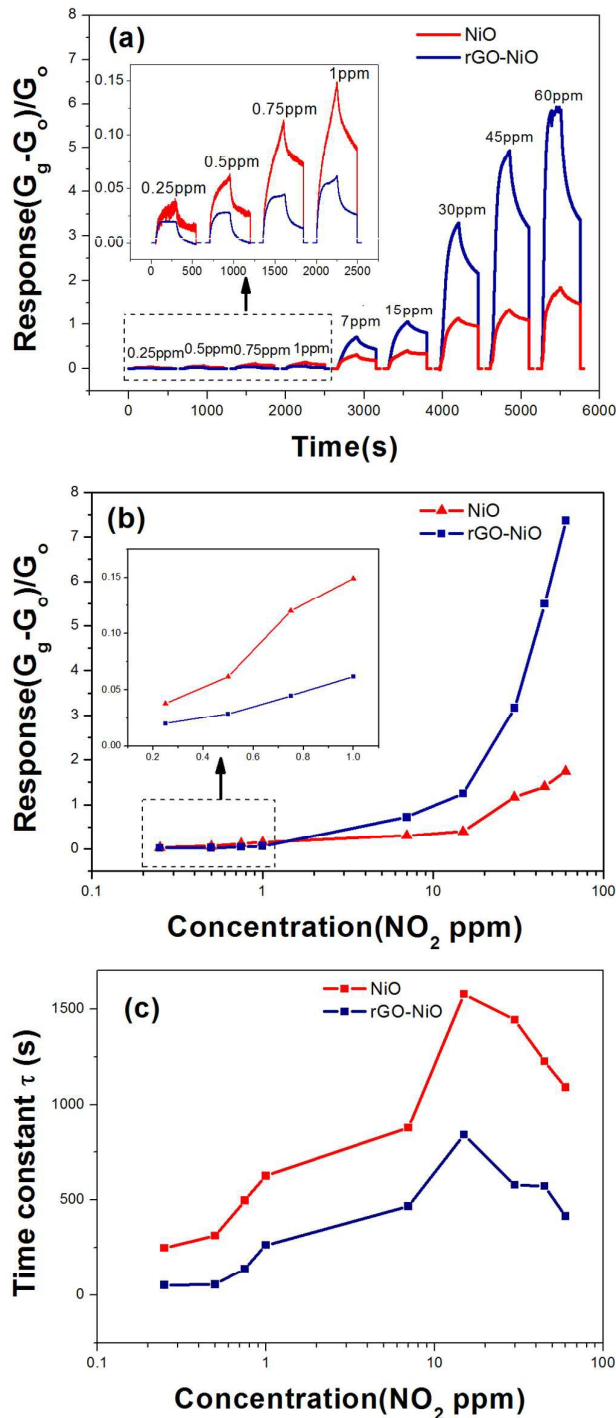


**Fig. 9** (a) Dynamic response-recovery curves of the pristine NiO and the rGO-NiO to the different concentration of  $\text{NO}_2$  at room temperature (the insert shows the magnified time-response curves in the low concentration range of 0.25-1 ppm). (b) The relationships between the  $\text{NO}_2$  concentration and the responses of the pristine NiO and the rGO-NiO (the insert shows the magnified response values in the low concentration range of 0.25-1 ppm). (c) The time constants of recovery curves of the pristine NiO and the rGO-NiO at different  $\text{NO}_2$  concentrations.

rGO-NiO in the whole concentration range, as shown in Fig. 9c, indicating that the incorporation of rGO into NiO effectively accelerates the recovery rate. In order to obtain the real recovery times of the pristine NiO and the rGO-NiO, the testing process was prolonged to make the conductivity of materials recover to its initial state, as shown in Fig. S1. According to the testing curves, the recovery times of the NiO to NO<sub>2</sub> at 0.25 ppm, 0.5 ppm and 0.75 ppm are 576 s, 720 s and 1146 s, and the recovery times of the rGO-NiO to the same concentration of NO<sub>2</sub> are 121 s, 129 s and 320 s, respectively. Meanwhile, the recovery curves of the NiO and the rGO-NiO to different concentration NO<sub>2</sub> were also fitted by eqn (1) to calculate the real recovery times of the NiO and the rGO-NiO in the whole range of NO<sub>2</sub> concentration, as shown in Fig. S2. The obtained real recovery times of the pristine NiO and the rGO-NiO are consistent with the measured real recovery times, and the real recovery times of the rGO-NiO are shorter than those of the pristine NiO. Though the response of the rGO-NiO is slightly inferior to the response of the NiO in the low NO<sub>2</sub> concentration range, the significantly enhanced response in the high concentration range and the accelerated recovery rate still comprehensively exhibit the improved sensing performances of the NiO-rGO.

Besides, the stability and the selectivity of the rGO-NiO are also taken into account. As shown in Fig. 10, the repeatable sensing properties of the NiO and the rGO-NiO to 0.5 ppm NO<sub>2</sub> exhibit their excellent stabilities. Moreover, each cycling recovery curves in Fig. 10 are also fitted by eqn (1), and the obtained time constants of the pristine NiO in each cycling are larger than those of the rGO-NiO (Fig. S3) that is consistent with the former results in Fig. 9c, indicating the improved recovery rate of the rGO-NiO. In order to evaluate the selectivity, the different target gases, such as NO<sub>2</sub>, CO, NH<sub>3</sub>, C<sub>2</sub>H<sub>5</sub>OH, HCHO and C<sub>6</sub>H<sub>6</sub>, are detected, as shown in Fig. 11(a). Among these target gases, both of the rGO-NiO and the NiO present the highest sensitive responses to NO<sub>2</sub>, indicating their outstanding selectivity. Additionally, the effect of humidity on the responses of the NiO and the rGO-NiO are also detailed in Fig. 11(b) and Fig. S4. A particularly interesting effect is the enhancement of the responses of the pristine NiO and the rGO-NiO to NO<sub>2</sub> in low humidity atmosphere. The similar phenomenon has also been observed by Hotovy et al.<sup>39</sup> However, the responses of the NiO and the rGO-NiO decrease with further increasing the humidity.

### 3.3. Room-temperature sensing mechanism of the pristine NiO

It is widely known that most of metal oxides have to be operated at elevated temperature when they are employed to detect toxic gases. In metal oxide semiconductors, there is an energy gap ( $E_g$ ) between filled (valence) and unfilled (conduction) electronic bands, which is appreciably greater than the thermal energy,  $K_B T = 0.0257$  eV, at room temperature (298 K).<sup>40</sup> Being different from the sensors operated at elevated temperature that the hot carriers determine the gas reaction on the surface of metal oxide, the room temperature sensing of NiO may be attributed to the reaction between the NO<sub>2</sub> molecules and the inherent defects of NiO. NiO is

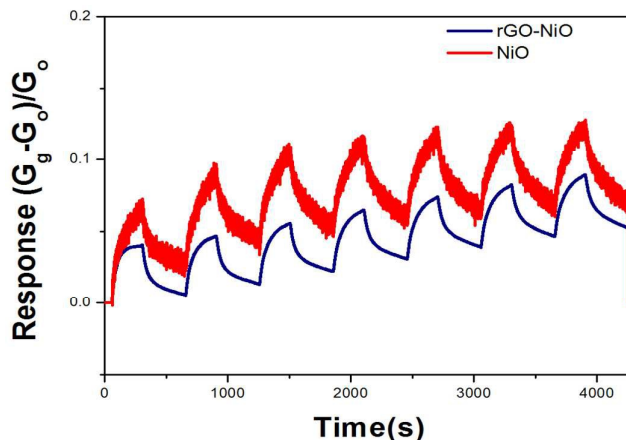


Fig. 10 The cycling response curves of the pristine NiO and the rGO-NiO to NO<sub>2</sub> at the concentration of 0.5 ppm.

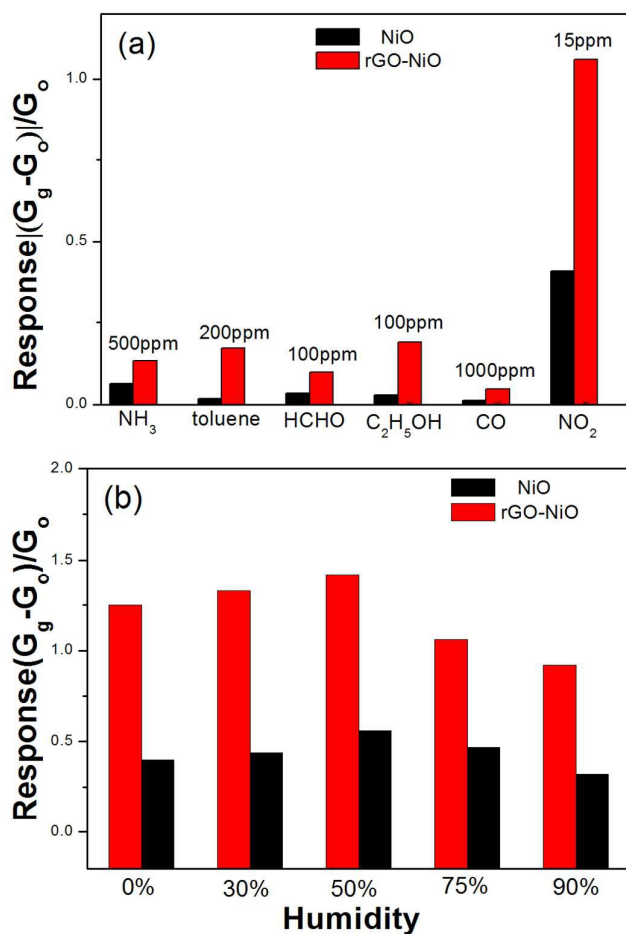


Fig. 11 (a) The response of the pristine NiO and the rGO-NiO nanocomposite towards various target gases at room temperature; (b) the responses towards 15 ppm NO<sub>2</sub> at different humidity.

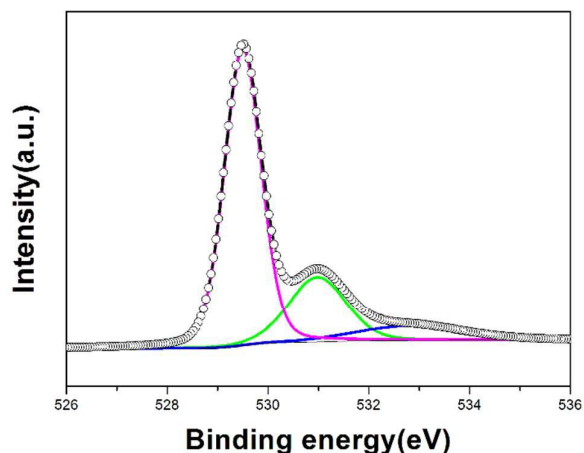
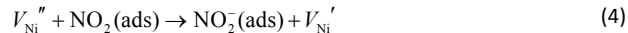


Fig. 12 The O 1s spectrum of the NiO.

a p-type semiconductor, in which vacancies occur in cation sites. For each cation vacancy, two  $\text{Ni}^{2+}$  at lattice sites are oxidized to  $\text{Ni}^{3+}$  to keep the electrical neutrality, thus there must be two electron holes formed from each vacancy.<sup>41</sup> In order to confirm the existence of  $\text{Ni}^{3+}$ , XPS spectrum of NiO was utilized, as shown in Fig. 12. Although the  $\text{Ni}^{2+}$  and  $\text{Ni}^{3+}$  oxide spectra are overlapped in the Ni 2p spectrum of NiO, a larger difference between  $\text{Ni}^{2+}$  and  $\text{Ni}^{3+}$  chemical bonds can be identified in the O 1s spectrum at 529.9 and 531.7 eV.<sup>42</sup> As shown in Fig. 12, the O 1s spectrum of as-prepared NiO can be deconvoluted into three peaks with binding energies of 529.569, 531.069 and 532.469 eV, corresponding to the binding states of  $\text{Ni}^{3+}$ ,  $\text{Ni}^{2+}$  and physisorbed  $\text{H}_2\text{O}$ . Therefore, the presence of  $\text{Ni}^{3+}$  indicates that the Ni vacancies exist in the non-stoichiometric NiO.

Ni vacancy, as a type of crystal imperfections, introduces a new shallow acceptor level in the band gap of NiO. When the as-prepared NiO is exposed to  $\text{NO}_2$  gas,  $\text{NO}_2$  extracts the electron from Ni vacancies. Therefore the adsorption of  $\text{NO}_2$  causes an increase in

the electrical hole density in NiO, and then increases the conductivity. The mechanism of Ni vacancies formation in NiO and the electronic interaction between the Ni vacancy and the adsorbed  $\text{NO}_2$  molecule are described in the following reactions,



where,  $V_{\text{Ni}}^{\cdot\prime}$  is the single negative charged Ni vacancy,  $V_{\text{Ni}}^{\prime\prime}$  is the doubly negative charged Ni vacancy. Because of the high adsorption energy and the drastic change of electronic structure, NiO is very sensitive to  $\text{NO}_2$  even at room temperature.<sup>43</sup> However, as shown in Fig. 9b, with increasing  $\text{NO}_2$  concentration, there is no significant increase in the sensitivity of the pristine NiO. The probable reason is that the adsorption of  $\text{NO}_2$  on the pristine NiO is easy to reach the saturation state due to the finite number of adsorption sites on the NiO surface. In other words, when the adsorption sites on the NiO surface are completely occupied by  $\text{NO}_2$  molecules, the following  $\text{NO}_2$  molecules have no strong electronic interaction with the NiO surface. Therefore, the further increase in the  $\text{NO}_2$  concentration gives little contribution to the increase in conductivity of the NiO because the  $\text{NO}_2$  adsorption reaches saturation on the NiO surface.

### 3.4. Comparative study on the $\text{NO}_2$ sensing mechanism between the NiO and the rGO-NiO

As shown in Fig. 9a and b, the rGO-NiO performs the remarkably enhanced sensitivity to  $\text{NO}_2$  in the high concentration range (7-60 ppm) compared to the NiO. However, in the low concentration range (0.25-1 ppm), the sensitivity of the rGO-NiO is slightly inferior to the pristine NiO. According to the above inverse gas-sensing behaviour in different  $\text{NO}_2$  concentration ranges, the related sensing mechanisms for the pristine NiO and the NiO-rGO nanocomposite are proposed in Fig. 13.

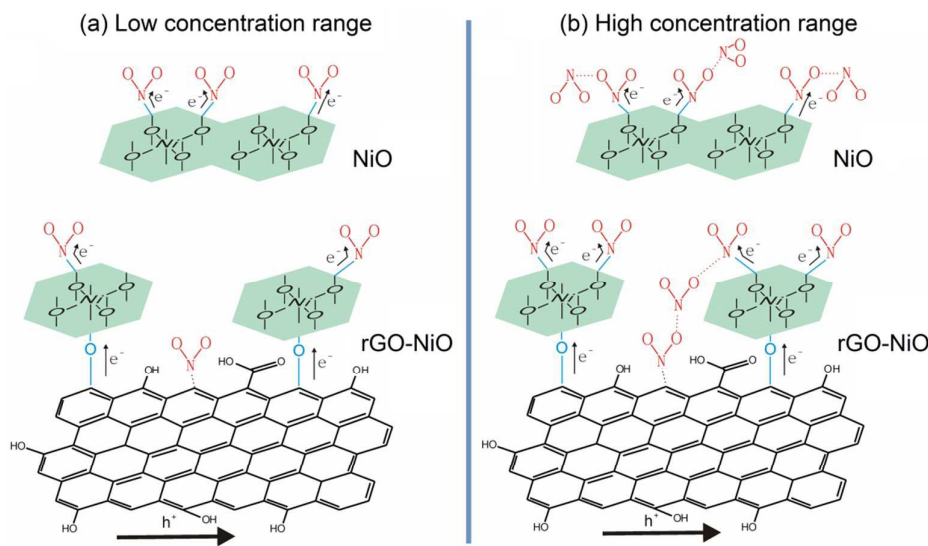


Fig. 13 Schematic illustration of the electron transfer of the adsorbed  $\text{NO}_2$  molecules on the NiO and the rGO-NiO in the low concentration range (a) and in the high concentration range (b).

In the low concentration range, the pristine NiO has enough active sites for NO<sub>2</sub> adsorption and reaction, and similarly the NiO assembled on the rGO can also offer enough active sites for NO<sub>2</sub> adsorption with electron transfer on the rGO-NiO nanocomposite. However, the rGO contains many dangling bonds and surface defects which also provide some adsorption sites for NO<sub>2</sub> adsorption. As shown in Fig. 8, the rGO has no response to NO<sub>2</sub>, because NO<sub>2</sub> molecules are physically adsorbed on the rGO and there is almost no electron transfer between the rGO and the adsorbed NO<sub>2</sub>. Therefore, the response of the pristine NiO in the low NO<sub>2</sub> concentration range is a little higher than the response of the rGO-NiO nanocomposite, since the physisorbed NO<sub>2</sub> on the rGO cannot arouse electron transfer and contribute to the sensing response.

In the high concentration range, the rGO-NiO nanocomposite performs the higher response and the faster recovery rate compared to the pristine NiO sensor. According to the morphological comparisons between the pristine NiO and the rGO-NiO nanocomposite, the aggregated NiO nanosheets can be clearly observed from the pristine NiO, however the dispersive NiO nanosheets tend to self-assemble on the rGO surface after incorporating the rGO in the nanocomposite. Additionally, the BET tests further confirm that the surface area of the rGO-NiO nanocomposite is ca. 3.6 times higher than that of the pristine NiO, meaning that the self-assembled NiO on the rGO surface may provide more effective active sites for NO<sub>2</sub> adsorption compared to the aggregated NiO.

According to the electronic structures, the similar work functions of the rGO (4.65–4.75 eV) and the NiO (5.0 eV) determine a low Schottky barrier so that the electron transfer can easily occur between the NiO and the rGO.<sup>44–46</sup> Moreover, the existing C–O–Ni bond between the NiO and the rGO is confirmed by the XPS results (Fig. 4d), which is also beneficial to the electron transfer between the NiO and the rGO. When the rGO-NiO is exposed to NO<sub>2</sub>, the adsorbed NO<sub>2</sub> molecules extract the electrons from the NiO, resulting in the Fermi level of the NiO shifting towards the valence band.<sup>47</sup> Therefore, at the interface between the NiO and the rGO, the existence of C–O–Ni bond and the lower Fermi level of the NiO promote more electrons to transfer from the rGO to the NiO. Since the NiO and the rGO exhibit the p-type behavior, the electrons are transferred from the rGO to the NiO and finally are extracted by the adsorbed NO<sub>2</sub> on NiO surface, resulting in the increase in the conductivity of the rGO-NiO nanocomposite. Moreover, it is different from the sensing mechanism in the low concentration range that the higher concentration of NO<sub>2</sub> promotes more NO<sub>2</sub> molecules to adsorb on the rGO surface in the nanocomposite. And the adsorbed NO<sub>2</sub> molecules on the rGO can diffuse and transfer from the rGO to the NiO *via* the concentration grads, and then participate in the electron exchange with the extra adsorption sites on the NiO. Since a large number of electrons are extracted from the rGO-NiO to the abundant surface-adsorbed NO<sub>2</sub>, the largely increased conductivity of the rGO-NiO arouses the much higher sensitivity in the high concentration range. Compared to the rGO-NiO, there are not enough active sites on the pristine NiO for NO<sub>2</sub> adsorption with increasing NO<sub>2</sub> concentration, thus the

physisorption and the chemisorption both take place on the NiO surface for the formation of a second ad-layer of NO<sub>2</sub> molecules. Therefore, the weak electron transfer between the second layer NO<sub>2</sub> molecules and the NiO results in the decreased sensitivity of the pristine NiO.

Commonly, it is very difficult to remove the adsorbed NO<sub>2</sub> molecules from the NiO surface because of the strong electronic interaction between the NO<sub>2</sub> molecules and the NiO.<sup>43</sup> Therefore, the NiO exhibits the very slow recovery rate, and it is very hard for NiO to recover its conductivity to the initial state after turning off the NO<sub>2</sub> gas. As shown in Fig. 9c, the recovery rate of the rGO-NiO is much higher than that of the pristine NiO, which could be attributed to the high electron mobility of the rGO. As suggested by the above results, the low barrier height and the existing C–O–Ni bond between the NiO and the rGO are beneficial to the electron transfer. Therefore, rGO, as a conductive network, its high electron mobility and the effective electron transfer with NiO facilitate the NO<sub>2</sub> detection through the change in the electrical conductivity of the hybrid nanostructure, leading to the higher recovery rate of the rGO-NiO.

#### 4. Conclusion

In this work, the self-assembled rGO-NiO nanocomposite was prepared by a simple solvothermal process. And a careful comparison study between the rGO-NiO nanocomposite and the pristine NiO for room temperature NO<sub>2</sub> sensing had been done. In the low NO<sub>2</sub> concentration range (0.25–1 ppm), the sensitivity of the pristine NiO was a little higher than that of the rGO-NiO nanocomposite, since a portion of NO<sub>2</sub> molecules physisorbed on the rGO cannot participate in the electron exchange with the rGO-NiO nanocomposite that decreased the sensitivity of the rGO-NiO. Inspiringly, the sensitivity of the rGO-NiO was obviously enhanced in the high concentration range (7–60 ppm) compared to the pristine NiO. The higher sensitivity of the rGO-NiO could be attributed to the effective electron transfer between the NiO and the rGO as well as the increase in the specific surface area of nanocomposite. Significantly, the rGO-NiO performed the accelerated recovery rate owing to the higher electron mobility of the rGO and the effective electron transfer between the NiO and the rGO. The present results indicate that the rGO-NiO nanocomposite has the immense potential as an alternative material for NO<sub>2</sub> sensing with high sensitivity and fast recovery rate. Through further understanding the room temperature gas-sensing mechanism, we hope this work is helpful for further improvement of graphene-based hybrid materials with even higher sensing performance at room temperature.

#### Acknowledgements

The authors gratefully acknowledge the financial support by the Aeronautical Science Foundation of China (Grant Nos. 20130379003). Moreover, we thank the technology support by the Analytic Testing Center of HUST for carrying out XRD, FESEM, HRTEM, and XPS.

## References

- S. Stankovich, D. A. Dikin, G. H. Dommett, K. M. Kohlhaas, E. J. Zimney, E. A. Stach, R. D. Piner, S. T. Nguyen and R. S. Ruoff, *Nature*, 2006, **442**, 282.
- P. T. Yin, T.-H. Kim, J.-W. Choi and K.-B. Lee, *Phys. Chem. Chem. Phys.*, 2013, **15**, 12785.
- D. A. C. Brownson and C. E. Banks, *Phys. Chem. Chem. Phys.*, 2012, **14**, 8264.
- E. Voloshina and Y. Dedkov, *Phys. Chem. Chem. Phys.*, 2012, **14**, 13502.
- S. M. Tan, A. Ambrosi, B. Khezri, R. D. Webster and M. Pumera, *Phys. Chem. Chem. Phys.*, 2014, **16**, 7058.
- X.-J. Zhu, J. Hu, H.-L. Dai, L. Ding and L. Jiang, *Electrochim. Acta*, 2012, **64**, 23.
- S. Mao, S. Cui, G. Lu, K. Yu, Z. Wen and J. Chen, *J. Mater. Chem.*, 2012, **22**, 11009.
- Y. Chang, Y. Yao, B. Wang, H. Luo, T. Li and L. Zhi, *J. Mater. Sci. Technol.*, 2013, **29**, 157.
- S. Cui, Z. Wen, E. C. Mattson, S. Mao, J. Chang, M. Weinert, C. J. Hirschmugl, M. Gajdardziska-Josifovska and J. Chen, *J. Mater. Chem. A*, 2013, **1**, 4462.
- X. He, J. Li, X. Gao and L. Wang, *Sens. Actuators, B*, 2003, **93**, 463.
- P. Xu, Z. Cheng, Q. Pan, J. Xu, Q. Xiang, W. Yu and Y. Chu, *Sens. Actuators, B*, 2008, **130**, 802.
- J. Kaur, V. D. Vankar and M. C. Bhatnagar, *Thin Solid Films*, 2010, **518**, 3982.
- S. Bai, X. Liu, D. Li, S. Chen, R. Luo and A. Chen, *Sens. Actuators, B*, 2011, **153**, 110.
- B. Shouli, C. Liangyuan, H. Jingwei, L. Dianqing, L. Ruixian, C. Aifan and C. C. Liu, *Sens. Actuators, B*, 2011, **159**, 97.
- S. Srivastava, K. Jain, V. N. Singh, S. Singh, N. Vijayan, N. Dilawar, G. Gupta and T. D. Senguttuvan, *Nanotechnol.*, 2012, **23**, 205501.
- S. Deng, V. Tjoa, H. M. Fan, H. R. Tan, D. C. Sayle, M. Olivo, S. Mhaisalkar, J. Wei and C. H. Sow, *J. Am. Chem. Soc.*, 2012, **134**, 4905.
- G. Lu, L. E. Ocola and J. Chen, *Appl. Phys. Lett.*, 2009, **94**, 083111.
- C. Luyo, R. Ionescu, L. F. Reyes, Z. Topalian, W. Estrada, E. Lobet, C. G. Granqvist and P. Heszler, *Sens. Actuators, B*, 2009, **138**, 14.
- M. Bao, Y. Chen, F. Li, J. Ma, T. Lv, Y. Tang, L. Chen, Z. Xu and T. Wang, *Nanoscale*, 2014, **6**, 4063.
- D. H. Nguyen and S. A. El-Safty, *Chemistry*, 2011, **17**, 12896.
- W. S. Hummers and R. E. Offeman, *J. Am. Chem. Soc.*, 1958, **80**, 1339.
- Q. Huang, D. Zeng, H. Li and C. Xie, *Nanoscale*, 2012, **4**, 5651.
- Y. Liao, H. Li, Y. Liu, Z. Zou, D. Zeng and C. Xie, *J. Comb. Chem.*, 2010, **12**, 883.
- G. S. Korotchenkov, V. I. Brinzari and S. V. Dmitriev, *SPIE*, 1998, **3539**, 196.
- G. Korotchenkov, V. Brinzari, V. Golovanov and Y. Blinov, *Sens. Actuators, B*, 2004, **98**, 41.
- K. Mukherjee and S. B. Majumder, *J. Appl. Phys.*, 2009, **106**, 064912.
- K. Mukherjee, D. C. Bharti and S. B. Majumder, *Sensors and Actuators B: Chemical*, 2010, **146**, 91.
- I. R. M. Kottegoda, N. H. Idris, L. Lu, J.-Z. Wang and H.-K. Liu, *Electrochim. Acta*, 2011, **56**, 5815.
- W. Wang, Y. Liu, C. Xu, C. Zheng and G. Wang, *Chem. Phys. Lett.*, 2002, **362**, 119.
- N. Mironova-Ulmane, A. Kuzmin, I. Steins, J. Grabis, I. Sildos and M. Pärs, *J. Phys.: Conf. Ser.*, 2007, **93**, 012039.
- B. Zhao, J. Song, P. Liu, W. Xu, T. Fang, Z. Jiao, H. Zhang and Y. Jiang, *J. Mater. Chem.*, 2011, **21**, 18792.
- F. Gao, D. Zeng, Q. Huang, S. Tian and C. Xie, *Phys. Chem. Chem. Phys.*, 2012, **14**, 10572.
- K. N. Kudin, B. Ozbas, H. C. Schniepp, R. K. Prud'homme, I. A. Aksay and R. Car, *Nano Lett.*, 2008, **8**, 36.
- S. Stankovich, D. A. Dikin, R. D. Piner, K. A. Kohlhaas, A. Kleinhammes, Y. Jia, Y. Wu, S. T. Nguyen and R. S. Ruoff, *Carbon*, 2007, **45**, 1558.
- H. Y. Jeong, D.-S. Lee, H. K. Choi, D. H. Lee, J.-E. Kim, J. Y. Lee, W. J. Lee, S. O. Kim and S.-Y. Choi, *Appl. Phys. Lett.*, 2010, **96**, 213105.
- C. Nethravathi and M. Rajamathi, *Carbon*, 2008, **46**, 1994.
- J. Zhang, X. Liu, L. Wang, T. Yang, X. Guo, S. Wu, S. Zhang and S. Wang, *Carbon*, 2011, **49**, 3538.
- G. Zhou, Da-Wei Wang, L.-C. Yin, N. Li, F. Li and H.-M. Cheng, *ACS Nano*, 2012, **6**, 3214.
- I. Hotovy, V. Rehacek, P. Siciliano, S. Capone and L. Spiess, *Thin Solid Films*, 2002, **418**, 9.
- J. A. Dirksen, K. Duval and T. A. Ring, *Sens. Actuators, B*, 2001, **80**, 106.
- G. Li, X. Wang, H. Ding and T. Zhang, *RSC Adv.*, 2012, **2**, 13018.
- S. Oswald and W. Brückner, *Surf. Interface Anal.*, 2004, **36**, 17.
- B. Wang, J. Nisar and R. Ahuja, *ACS Appl. Mater. Interfaces*, 2012, **4**, 5691.
- M. T. Greiner, M. G. Helander, Z.-B. Wang, W.-M. Tang and Z.-H. Lu, *J. Phys. Chem. C*, 2010, **114**, 19777.
- J. Olivier, B. Servet, M. Vergnolle, M. Mosca and G. Garry, *Synth. Met.*, 2001, **122**, 87.
- Y.-J. Yu, Y. Zhao, S. Ryu, L. E. Brus, K. S. Kim and P. Kim, *Nano Letters*, 2009, **9**, 3430.
- G. Lu, L. E. Ocola and J. Chen, *Adv. Mater.*, 2009, **21**, 2487.